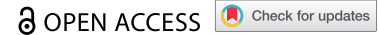








REPORT



## Improved epitope resolution of the prefusion trimer-specific antibody AM14 bound to the RSV F glycoprotein

Wayne Harshbarger <sup>1</sup>, Priyanka D. Abeyrathne <sup>1</sup>, Sai Tian , Ying Huang<sup>†</sup>, Sumana Chandramouli <sup>#</sup>, Matthew James Bottomley , and Enrico Malito <sup>‡</sup>

GSK, Vaccine Design and Cellular Immunology, Rockville, MD, USA

### ABSTRACT

Respiratory syncytial virus (RSV) is the most common cause of acute lower respiratory tract infections resulting in medical intervention and hospitalizations during infancy and early childhood, and vaccination against RSV remains a public health priority. The RSV F glycoprotein is a major target of neutralizing antibodies, and the prefusion stabilized form of F (DS-Cav1) is under investigation as a vaccine antigen. AM14 is a human monoclonal antibody with the exclusive capacity of binding an epitope on prefusion F (PreF), which spans two F protomers. The quality of recognizing a trimer-specific epitope makes AM14 valuable for probing PreF-based immunogen conformation and functionality during vaccine production. Currently, only a low-resolution (5.5 Å) X-ray structure is available of the PreF-AM14 complex, revealing few reliable details of the interface. Here, we perform complementary structural studies using X-ray crystallography and cryo-electron microscopy (cryo-EM) to provide improved resolution structures at 3.6 Å and 3.4 Å resolutions, respectively. Both X-ray and cryo-EM structures provide clear side-chain densities, which allow for accurate mapping of the AM14 epitope on DS-Cav1. The structures help rationalize the molecular basis for AM14 loss of binding to RSV F monoclonal antibody-resistant mutants and reveal flexibility for the side chain of a key antigenic residue on PreF. This work provides the basis for a comprehensive understanding of RSV F trimer specificity with implications in vaccine design and quality assessment of PreF-based immunogens.

### ARTICLE HISTORY

Received 7 May 2021  
Revised 30 June 2021  
Accepted 12 July 2021

### KEYWORDS

RSV; antigen; antibody; vaccine; epitope; structural vaccinology; cryo-EM

### Introduction

Human respiratory syncytial virus (RSV) is a negative-sense, enveloped, RNA virus that causes respiratory tract infections.<sup>1</sup> Newborns, children, and the elderly are high-risk populations for severe lower respiratory tract infections mediated by RSV.<sup>2</sup> As a major unmet medical need, RSV has been a high priority for vaccine development for several decades.<sup>3</sup> While there is still no licensed vaccine available against RSV, several programs are currently in clinical development.<sup>4,5</sup>

The native F antigen is synthesized as an inactive precursor (F0) that becomes active upon cleavage by a furin-like protease into subunits F1 and F2, resulting in the release of peptide p27. RSV F is a metastable, trimeric class I fusion protein anchored to the viral surface and capable of spontaneously and irreversibly changing conformation from a pre- (PreF) to a post-fusion (PostF) form to facilitate fusion of the viral envelope with the host membrane.<sup>6</sup> Of the recombinant antigens used in ongoing clinical studies, one is a pre-fusion-stabilized form of the RSV fusion antigen F, known as DS-Cav1<sup>7</sup> due to engineering of a disulfide (DS) bond and cavity-filling (Cav) mutations,

which also has a C-terminal ‘foldon’ domain for additional stabilization of the trimer.<sup>8</sup> In clinical trials, several vaccine development efforts that used a PostF antigen failed to provide adequate protection,<sup>9</sup> whereas use of the engineered PreF DS-Cav1 molecule has been shown to elicit high neutralizing titers.<sup>10</sup> Moreover, PreF is the primary target of neutralizing antibodies (nAbs) induced during natural infection and capable of efficiently depleting protective anti-RSV antibodies in human sera.<sup>11</sup>

Conformation-dependent access to neutralizing epitopes on the surface of F has been demonstrated, revealing the presence of at least four distinct “antigenic sites” that can either be shared between PreF and PostF (e.g., site II, bound by palivizumab and motavizumab, and site IV, bound by 101F),<sup>12–15</sup> or that are present exclusively on PreF (e.g., site Ø, bound by D25, and site V, bound by hRSV90, CR9501, and RSB1). Importantly, sites that are only present on PreF are targeted by the more potent neutralizing antibodies known so far, while sites present on either PreF only or both PreF and PostF encompass majority of the human B-cell repertoire for RSV.<sup>16–18</sup>

**CONTACT** Enrico Malito  [wayne.d.harshbarger@gsk.com](mailto:wayne.d.harshbarger@gsk.com)  GSK, Vaccine Design and Cellular Immunology, Rockville, MD, USA


<sup>1</sup>These authors contributed equally to this work

<sup>†</sup>Current address: Merck Research Laboratories, Merck & Co., Inc., Kenilworth, NJ

<sup>#</sup>Current address: Moderna Therapeutics Inc., Cambridge, MA, United States of America

<sup>‡</sup>Current address: Schrödinger, Inc., 120 West 45th St., New York, NY 10036, USA

Abbreviations: CDR: Complementarity-determining region; cryo-EM, cryo-electron microscopy; Fab, fragment antigen binding; FSC, fourier shell correlation; HCDR, heavy complementarity-determining region; HF, heavy chain framework; LCDR, light complementarity-determining region; LF, light chain framework; mAb, monoclonal antibody; nAb, neutralizing antibody; PDB, protein data bank; PreF, pre-fusion; PostF, post-fusion; RSV, respiratory syncytial virus.

 Supplemental data for this article can be accessed on the [publisher's website](#)

© 2021 Taylor & Francis Group, LLC

This is an Open Access article distributed under the terms of the Creative Commons Attribution-NonCommercial License (<http://creativecommons.org/licenses/by-nc/4.0/>), which permits unrestricted non-commercial use, distribution, and reproduction in any medium, provided the original work is properly cited.

The monoclonal antibody (mAb) AM14 is a potent RSV neutralizing antibody that recognizes a quaternary epitope on the trimeric PreF protein,<sup>19</sup> thus of major interest as a key reagent for probing the antigen trimeric state during vaccine development. Undoubtedly, high-resolution epitope mapping plays a critical role in vaccine research and development projects.<sup>20</sup> Information on antigen-antibody interactions usually guides the rational design of antigens and antibodies that can elicit desired neutralizing or protective responses, while also providing insights into functional regions. Previously, only low-resolution (5.5 Å) information on the AM14 epitope of PreF was obtained from a crystal structure of a ternary complex between DS-Cav1 and antigen-binding fragments (Fabs) of AM14 and motavizumab.<sup>19</sup> Although the positioning of AM14 was supported by the generation of mAb-resistant mutants (MARMs), the lack of side-chain densities resulted in an incomplete analysis of specific interactions. In this study, we sought to improve the resolution of the AM14 epitope on DS-Cav1, so that we could precisely delineate antibody/antigen contacts, and at the same time compare resolutions achievable by complementary 3D structure determination methods. For this, we solved both X-ray and cryo-EM structures of the DS-Cav1-FabAM14 complex, at 3.6 and 3.4 Å resolution, and below we describe and discuss the implications of high-resolution structure determination, using orthogonal methods, for vaccine design.

## Results

### Improved resolution of the DS-Cav1-AM14 complex by X-ray and cryo-EM

To better understand the RSV PreF epitope targeted by mAb AM14, we determined the crystal structure of DS-Cav1 bound by Fab AM14 at 3.6 Å resolution (Figure 1a), a ~2 Å improvement over previously published data.<sup>19</sup> The complex crystallized in a buffer condition which was different from that of the previously reported structure (see Methods), and diffraction data were scaled into space group C2 with the asymmetric unit found to contain one DS-Cav1 trimer bound by three copies of Fab AM14. The structure was solved by molecular replacement (see Methods), and the final coordinates refined to  $R_{\text{work}}/R_{\text{free}}$  values of 20/24% (Table 1). Clear electron densities for backbone and side-chain residues were observed throughout the majority of the complex, especially at the DS-Cav1-AM14 interface (Figure 2a), an improvement to the previously determined lower resolution structure. In the current structure, areas of disorder/weak electron density and high B-factors include the Fab constant portions, helices near the foldon (the foldon is not visible in the crystal structure), and the DS-Cav1 apex (site Ø) (Figure 2b), which is often the case for structures not stabilized by Fabs of site Ø-directed mAbs.<sup>8</sup>

Simultaneous with the X-ray structure, we also successfully used single-particle cryo-EM to improve the resolution of the DS-Cav1-AM14 structure. During single particle image processing, DS-Cav1-AM14 particles were extracted from micrographs and used for 2D classification, which revealed clear, high-resolution secondary structural details of the DS-Cav1 trimer and three copies of the Fab AM14 (Figure 1b). The 3D

reconstruction of the DS-Cav1-AM14 complex was solved, *ab-initio*, from a single dataset using cisTEM image processing software, resulting in a global resolution of 3.4 Å according to the Fourier shell correlation (FSC) at 0.143 (Figure 1c and Supplementary Figure 1). Local resolution limits for the map indicate a maximum resolution of ~5 Å for the Fab AM14 constant regions as well as for the DS-Cav1 foldon domain, and ~4 Å for DS-Cav1 site Ø, which is consistent with the interpretation from the X-ray structure that these regions are either flexible or disordered (Supplementary Figure 1c). Resolution for the paratope/epitope region is in the 3.5–4 Å range, while resolution in the core of DS-Cav1 extends to 3 Å.

To select the best model for refinement in the EM map, the previously published 5.5 Å X-ray structure (PDB 4ZYP), the 3.6 Å X-ray structure from this study, as well as coordinates of post fusion F (PDB 3RKI) were docked into the EM map using Chimera.<sup>21</sup> As expected, both pre-F structures fit the density well, confirming that the elongated density of DS-Cav1 determined by cryo-EM is due to the trimerization (foldon) domain and not to a post-fusion conformation of F (Supplementary Figure 2). While both coordinates of the DS-Cav1 and the AM14 variable regions derived from either the low resolution or new X-ray structures docked well into the cryo-EM map (cross-correlation = 0.36 for each), we used the high-resolution X-ray structure solved in this study for further refinement in Phenix<sup>22</sup> and Coot<sup>23</sup> (Table 2).

Superpositions of the final refined cryo-EM structure onto either the X-ray structure solved in this study or the previously reported X-ray structure at low resolution (PDB 4ZYP) resulted in RMSDs of ~0.6 Å across 373 C<sub>α</sub> atoms, with near perfect agreement for the AM14 heavy chain complementarity-determining region (CDR) positions with respect to DS-Cav1 (Supplementary Figure 3). Slight deviations observed in light-chain CDRs and the heavy- and light-chain Fab constant regions between the structures could be attributed to the influence of crystal packing. Unique to the EM structure are densities for glycans at all three Asn500 locations (only visible for a single Asn500 in X-ray structure) and the foldon trimerization domain of DS-Cav1 (Figure 1c).

Overall, the high quality of both the cryo-EM and X-ray densities obtained in this study are comparable, particularly in the AM14 CDRs and the DS-Cav1 epitope (Figure 3). This provides confidence for interpreting the interactions discussed hereafter, and for allowing us to discern subtle differences in amino acid orientations between the bound and unbound states for both AM14 (PDB 4ZYK) and DS-Cav1 (PDB 4MMU).

### High-resolution mapping of DS-Cav1-AM14 interactions

The improved resolutions provided by each structure allowed for precise epitope mapping of the AM14 binding site, which was performed using the Protein Interface and Surface Accessibility (PISA) server.<sup>24</sup> For simplicity, and due to the near identical features revealed by our X-ray and cryo-EM structures, our analyses refer to the X-ray structure unless otherwise stated. AM14 uses a combination of heavy- and light-chain CDRs to simultaneously contact portions of two DS-Cav1 protomers, consistent with previous reports.<sup>19</sup> This is

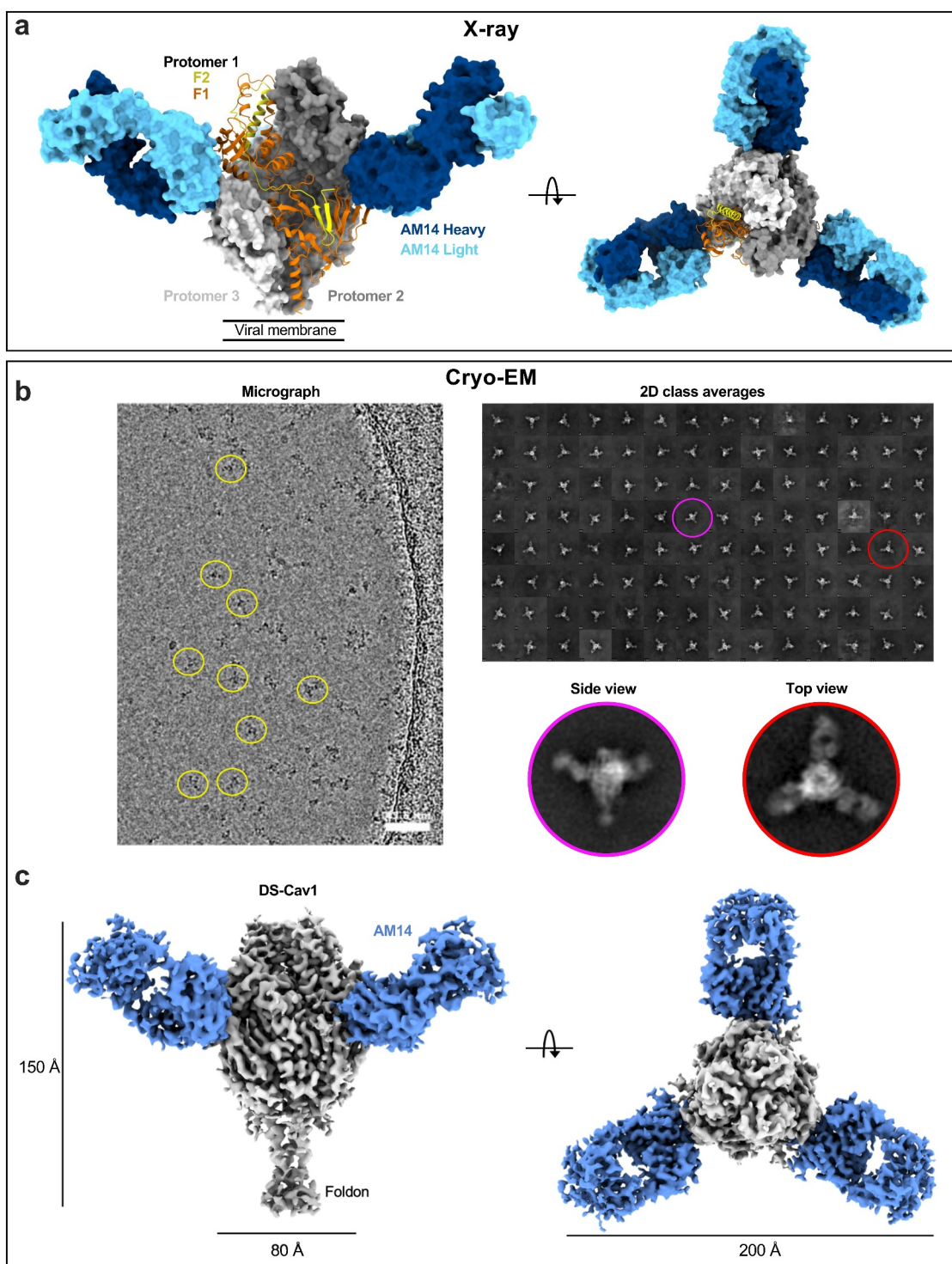


**Figure 1. Structures of DS-Cav1 bound by Fab AM14.** (a) X-ray crystal structure of DS-Cav1 bound by Fab AM14 from a front view and rotated 90 degrees toward the plane of view. The primary DS-Cav1 protomer which is bound by AM14 is shown as cartoon and colored gold for the F2 domain and orange for the F1 domain. The second protomer of DS-Cav1 which is contacted by AM14 is shown in surface and colored dark gray, while the third DS-Cav1 protomer is colored white. The Fab AM14 is shown in surface with the heavy-chain colored dark blue and the light-chain colored cyan. (b) Top left image shows representative motion-corrected cryo-EM micrograph of DS-Cav1-AM14 protein embedded in a thin layer of vitreous ice. Particles are highlighted in yellow circles, scale bar: 43.5 nm. Top right: 2D class averages showing side (purple circle) and top (red circle) views, which are also shown zoomed in the circles below. (c) The 3.4 Å cryo-EM map of the DS-Cav1-AM14 complex with three DS-Cav1 protomers colored in light gray and three Fab AM14 molecules colored in blue.

in contrast to other structures of human antibodies bound to PreF, which all recognize a single F protomer. Some nAbs, such as RSB1 and D25, do make minor contacts with a second F protomer; however, they bind with high affinity to

monomeric F, thereby distinguishing them from the unique trimer specificity of AM14. Despite binding across two F protomers, the location of the AM14 epitope is highly conserved among RSV A and B strains (Supplementary Figure 4),

**Table 1.** X-ray data collection and refinement statistics.

	PDB 7MMN
<b>Data Collection</b>	
Wavelength (Å)	1
Resolution range (Å)	41.08–3.57 (3.70–3.57) *
Space group	C2
Cell dimensions	
<i>a</i> , <i>b</i> , <i>c</i> (Å)	223.4, 183.0, 135.8
$\alpha$ , $\beta$ , $\gamma$ (°)	90, 103, 90
Total reflections	225376 (20224)
Unique reflections	62699 (2848)
Multiplicity	3.6 (3.3)
Completeness (%)	88.2 (45.1)
<i>I</i> / $\sigma$ <i>I</i>	8.3 (1.7)
Wilson B-factor	49.78
R-merge	0.215 (0.892)
CC <sub>1/2</sub>	0.96 (0.51)
<b>Refinement</b>	
Resolution (Å)	41.08–3.57
No. reflections	55716
R <sub>work</sub> /R <sub>free</sub> (%)	20/24
No. protein atoms	20370
No. of ligand residues	
NAG	1
GOL	1
R.m.s. deviations:	
Bond lengths (Å)	0.003
Bond angles (°)	0.65
Ramachandran plot <sup>#</sup>	
Favored (%)	94.4
Allowed (%)	5.41
Outliers (%)	0.19
Average B-factor	50.73
Macromolecules	50.72
Ligands	60.72

R.m.s. deviation, root-mean square deviation.

\*Values in parentheses are for the highest resolution shell.

<sup>#</sup>Measured using Molprobitry

as also apparent by the similar neutralization potency toward strains from either subtype (RSV subtype A: IC<sub>50</sub> = 15.1 ng/mL; RSV subtype B: IC<sub>50</sub> = 11.0 ng/mL).<sup>19</sup>

The AM14 epitope located on the DS-Cav1 membrane-proximal protomer (hereafter referred to as protomer 1) encompasses 531 Å<sup>2</sup> on F1 from residues Asn426 to Lys465, while the membrane distal protomer (protomer 2) has a buried surface of 297 Å<sup>2</sup> from F1 residues Lys156 through Gly184. (Figure 4a-d). A large portion of these contacts are mediated by the 16-residue HCDR3, which buries a total surface of 397 Å<sup>2</sup> across the two protomers (273 Å<sup>2</sup> on protomer 1 and 124 Å<sup>2</sup> on protomer 2), with residues Ile101<sub>HCDR3</sub>, Val102<sub>HCDR3</sub>, and Asp103<sub>HCDR3</sub> binding a groove between the two protomers. His31<sub>HCDR1</sub> also recognizes a groove between the protomers, burying 66 Å<sup>2</sup> on protomer 1 and 123 Å<sup>2</sup> on protomer 2 (Figure 4b). The majority of the light-chain buried surface on DS-Cav1 is attributed to LCDR1 and LCDR3 interactions with protomer 1, whereas light-chain framework 2 (LF2) and LF3 each bury a single residue on protomer 2, and no contacts are made with LCDR2.

DS-Cav1-AM14 interactions stemming from contacts between the AM14 HCDR2, LCDR1, LF2, and LF3 portions were not previously identified. Specifically, we found that protomer 1 residues Lys445 and Glu463 form hydrogen bonds with Tyr53<sub>HCDR2</sub> (Figure 4e), while Tyr32<sub>LCDR1</sub> traps DS-Cav1 residue Arg429 between the AM14 heavy and light chains by forming a hydrogen bond with the Arg429 main chain

oxygen (Figure 4f). Additionally, for protomer 2, LF-mediated contacts result from the side chains of His49<sub>LF2</sub> and Thr56<sub>LF3</sub> that extend toward Ser180 and Lys166, respectively, on DS-Cav1, thus both favorably positioned for electrostatic interactions (Figure 4g). Notably, His49<sub>LF2</sub> is the result of a somatic hypermutation (SHM), with an inferred germline configuration of tyrosine (IMGT/V-QUEST).<sup>25</sup> Histidine in this position can maintain a polar interaction with Ser180 while also likely preventing a steric clash that may occur with the larger germline tyrosine. Other AM14 inferred SHMs making interactions with DS-Cav1 are located on the heavy chain and include Glu56<sub>HCDR2</sub> (mutated from serine), Ser28<sub>HCDR1</sub> (mutated from threonine), and the above-mentioned His31<sub>HCDR2</sub> (mutated from serine), which binds between the two F protomers (Figure 4a). Together, these results provide a greatly enhanced understanding of the antigen/antibody interface, allowing clear mechanistic insights into the unique nature of the prefusion trimer-specific antibody, AM14.

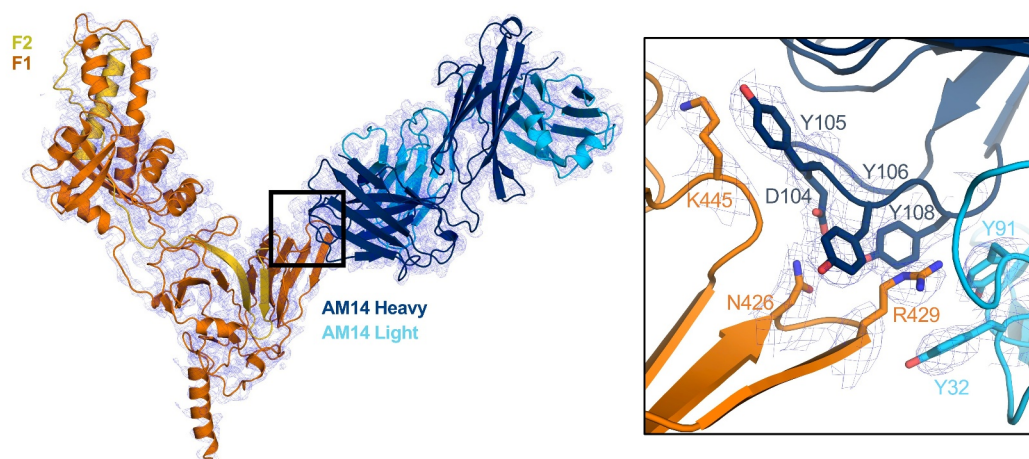
### Molecular basis for monoclonal antibody-resistant mutants

Four MARMs (L160S, N183K, N426D, and R429S) were previously generated in RSV F to validate the AM14 epitope.<sup>19</sup> These mutations interfere with key AM14 interactions and provide potential RSV escape mechanisms from AM14-like antibodies. Given the improved resolution for side-chain interactions, we examined these contacts to better understand these critical antibody/antigen interactions and the role these residues play in PreF antigenicity.

Leu160 is located on the loop connecting helices  $\alpha$ 2 and  $\alpha$ 3 and recognizes a hydrophobic pocket formed by side chains of AM14 residues Val102<sub>HCDR3</sub>, Tyr32<sub>HCDR1</sub>, and His31<sub>HCDR1</sub> (Figure 5a). Mutation of the hydrophobic leucine to a polar serine would result in loss of van der Waal contacts (vdWs) with each of these residues, thus explaining the observed loss in binding. In the case of MARM Asn183Lys, which is located on the loop connecting  $\beta$ 3– $\beta$ 4, the asparagine side chain is facing inwards toward the PreF core and with the aliphatic side chain likely contributing to vdWs contacts with the side chain of Val102<sub>HCDR3</sub> (Figure 5a). A lysine at this position may be unable to bury in the core of PreF, resulting in solvent exposure of the side chain and a steric clash with the AM14 heavy chain. Alternatively, if the mutated lysine were able to bury in the core of PreF, it may lead to a structural perturbation of the trimer and alter the conformation necessary for binding by AM14.

Mutants Asn426Asp and Arg429Ser are each located on the loop connecting  $\beta$ 17– $\beta$ 18 and are found to be involved in extensive H-bonding interactions with AM14 (Figure 5b). The mutation Asn426Asp would lead to a loss of charge complementarity and likely loss of a salt bridge with Asp100<sub>HCDR3</sub>. Nearby, the Arg429 side chain was found to extend between the AM14 heavy- and light-chain CDRs into a pocket surrounded by four tyrosine residues (two each from the AM14 heavy and light chains), revealing up to four hydrogen bond interactions as well as multiple vdWs contacts (Figure 5b). This conformation of the Arg429 side chain places the guanidinium moiety ~9 Å from the location in the lower resolution X-ray structure, for which no density was present for discerning the proper

a



b

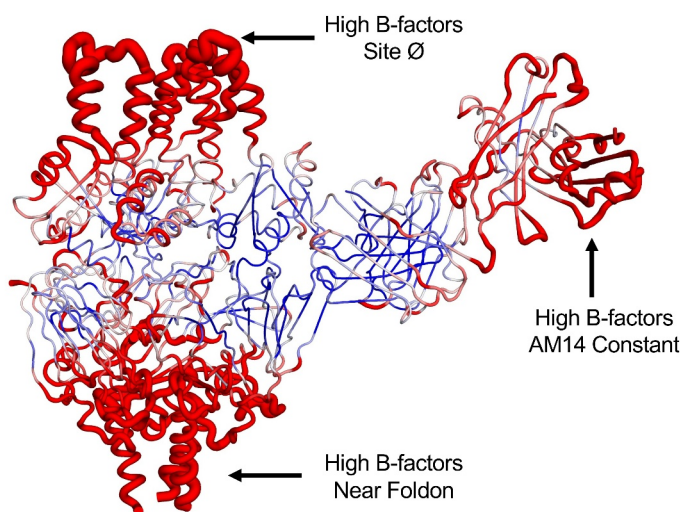


**Figure 2.** (a) 2Fo-Fc electron densities (contoured at  $1\sigma$ ) are shown as mesh around one protomer of DS-Cav1 in complex with one AM14 Fab, as well as zoomed at the heavy- and light-chain interface with DS-Cav1. (b) The DS-Cav1 trimer and one AM14 Fab are shown in cartoon tube and colored according to B-factors with red thick tubes indicating high B-factors and thin blue or white tubes indicating average or low B-factors.

orientation (Supplementary Figure 5). Notably, when compared to the unbound DS-Cav1 X-ray structure (PDB 4MMU) for which there is electron density present, the Arg429 side chain is again found in a conformation that this time places the guanidinium moiety  $\sim 4$  Å from the location found in our AM14 bound structure, thus indicating plasticity and free rotation of the Arg429 side chain. Additionally, there is an  $\sim 3$  Å shift for the side chain of AM14 residue Tyr106<sub>HCDR3</sub> and rearrangement of the LCDR3 backbone when compared to the AM14 unbound state (PDB 4ZYK), each of which prevents a steric clash with Arg429 (Supplementary Figure 5c).

#### **AM14 competes with antigenic sites IV and V**

The quaternary epitope recognized by AM14 is located below antigenic site Ø (when F is viewed along a vertical axis passing through site Ø), and because the AM14 angle of approach is nearly perpendicular to PreF, it does not compete with site Ø

directed mAbs such as D25. The AM14 epitope is sandwiched between antigenic sites IV and V, and thus competition with 101F (site IV) as well as RSB1 (site V) has been reported.<sup>26</sup> In order to better understand the footprint of the AM14 epitope as it relates to the epitopes for these surrounding mAbs, and thus elucidate the molecular basis for AM14 competition across multiple antigenic sites, we superimposed our DS-Cav1-AM14 structure with the RSB1 complex (PDB 6W52), the D25 complex (PDB 4JHW), and the 101F-17-mer X-ray structure (PDB 3O45) (Figure 6).

The AM14 and 101F epitopes overlap significantly around residues 427–432, which are located on sheet  $\beta 17$  and the loop connecting  $\beta 17$  and  $\beta 18$ , as also reported previously,<sup>28</sup> which thus explains the strong binding competition between these antibodies. Interestingly, Arg429 assumes a different conformation when bound by 101F, with the side-chain guanidinium moiety shifted by  $\sim 4$  Å compared to the AM14 bound structure (Supplementary Figure 5b). This orientation positions the

**Table 2.** Cryo-EM data collection and refinement statistics.

	EMDB: EMD-23933/PDB: 7MPG
<b>Data collection</b>	
Microscope	ThermoFisher Krios
Acceleration voltage [kV]	300
Detector	Falcon III
Physical pixel size [Å]	1.07
Electron exposure [e <sup>-</sup> /Å <sup>2</sup> ]	26.7
Total exposure [s]	60
Number of frames (per movie)	75
Movies acquired	1353
<b>Image processing</b>	
Movies processed	1078
Pixel size for processing and reconstruction [Å]	1.07
Box size [pixels <sup>2</sup> ]	400
Number of particles picked	26,936
Number of particles 2D classification	25,280
Number of particles 3D classification	23,737
Symmetry	C3
Global resolution (FSC = 0.143)	3.4 Å
<b>Model building and refinement</b>	
Atoms	40463
Protein residues	2640
Ligand residues (NAG)	3
Bond lengths (Å)	0.003
Bond angles (°)	0.63
<b>Validation</b>	
MolProbity score	1.97
Clashscore	12.41
<b>Ramachandran plot</b>	
Favored (%)	94.75
Allowed (%)	5.13
Outliers (%)	0.11

Arg429 side chain between two 101F HCDR3 tyrosine side chains. Indeed, an Arg429Ser escape mutant has also been described for 101F,<sup>27,29,30</sup> suggesting that flexibility of the Arg429 side chain is a key attribute for binding to either epitope.

Fab RSB1 recognizes portions of F2 on helix  $\alpha$ 1 with heavy chain CDRs, and helices  $\alpha$ 2-3 on the F1 subunit with light-chain CDRs. These latter contacts appear to be the cause for the observed epitope competition, as both RSB1 and AM14 bury ~40% of the accessible surface area on opposite faces of a Glu (residue 161) sidechain (Figure 6). It is plausible that a steric clash between the AM14 and RSB1 variable fragments is responsible for the observed competition.

## Discussion

AM14 is a human mAb that recognizes a quaternary, prefusion trimer-specific epitope on RSV PreF. Several clinical trials are currently underway to evaluate the safety and efficacy of vaccination with various PreFusion stabilized F antigens in pregnant, infant, and elderly populations.<sup>31</sup> Due to its unique binding characteristics, AM14 is an attractive antibody for use as a biochemical tool to ensure that PreF retains a trimeric conformation during vaccine production. As such, it is crucial to have a thorough structural understanding of the AM14 mode of recognition, which was not fully possible from the previously reported 5.5 Å X-ray structure<sup>19</sup> due to poor definition of the antigen/antibody interface.

In this study, we used both X-ray crystallography and single particle cryo-EM to further enhance our understanding of the

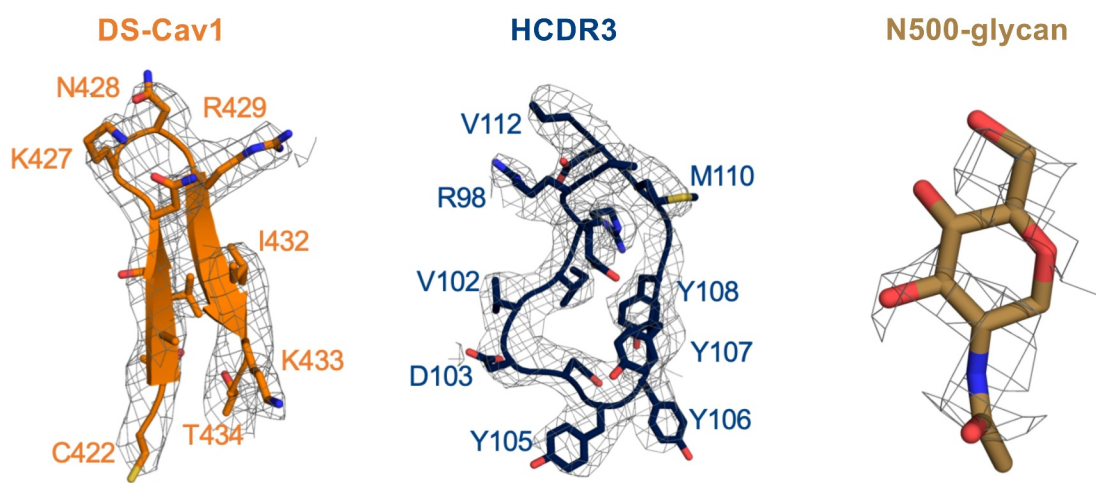
interactions that drive trimer specificity, as well as to gain new insights into antigenic details related to MARMs, and orientations of residues at the paratope/epitope interface. Stabilization of the PreF form of the RSV F protein (DS-Cav1) has enabled 3D structure determination and the elucidation of epitopes for antibodies targeting a plethora of antigenic sites.<sup>17,28</sup> The recent emergence of single-particle cryo-EM has allowed the solution of medium-to-high-resolution structures of antibody-antigen complexes for viruses such as HIV,<sup>32–36</sup> influenza,<sup>37–40</sup> and Dengue,<sup>41–43</sup> as well as for an RSV PostF-FabR4.C6 complex,<sup>44</sup> and most recently vaccine-elicited antibodies bound to DS-Cav1.<sup>45</sup> Using single particle cryo-EM, we were able to achieve an overall resolution of 3.4 Å, which produced a 3D reconstruction of comparable quality to a 3.6 Å DS-Cav1-AM14 X-ray structure also reported here. This represents another important case of the application of the rapidly evolving cryo-EM technology for the high-resolution characterization of vaccine antigen targets. In addition to resolutions comparable with those routinely obtained by X-ray crystallography, a key advantage of cryo-EM is the lack of dependency from crystals and therefore the lack of the stabilizing effect of the crystal environment. This can enable the elucidation of variable resolutions, which in turn might provide insights into the dynamics of a macromolecule. Here, we showed how the local resolution of the DS-Cav1-FabAM14 cryo-EM structure correlates well with the B-factors distribution observed from the x-ray crystal structure of the same complex and at a comparable overall resolution, thus indicating the presence of similar regions of flexibility or local disorder.

While the overall binding orientation of AM14 to DS-Cav1 observed from the structures solved in this study is consistent with the previously reported structure,<sup>19</sup> the improved resolutions allowed the unambiguous identification of specific side-chain interactions in the AM14 CDRs as well as framework regions, and therefore a better understanding for the antigenicity of this unique epitope. Importantly, visible electron densities for amino acid side chains on DS-Cav1 revealed the correct orientation for Arg429, which we found extends between the AM14 heavy- and light-chain CDRs and makes multiple hydrogen bonds, thus explaining the loss of binding for MARM, Arg429Ser. Interactions for additional MARMs (Leu160Ser, Asn183Lys, and Arg429Ser) were also rationalized or confirmed based on our improved structures.

Our study highlights the reorientation of Arg429 when PreF is bound by either AM14 or 101F. This side-chain flexibility is comparable to that seen when RSV PreF is bound by antibodies RSB1 or CR9501, which each recognizes antigenic site V.<sup>26</sup> In the case of these antibodies, the Lys65 side chain on PreF can assume different conformations in order to be positioned at the interface of the heavy- and light-chain CDRs for either antibody, while Lys87, Glu66, and Asn63 are also significantly displaced in the antibody-bound states. Additionally, CR9501 appears to “splay open” the PreF trimer, suggesting an “induced fit” mechanism for antibody binding. In our current structure, the reorientation of Arg429 may be the result of “conformational selection,”<sup>46</sup> rather than induced fit, whereby the Arg429 side chain naturally samples several conformations before being stabilized by either the AM14 or 101F bound states; however, more work is needed to fully clarify the

a

## Cryo-EM densities



b

## X-ray densities

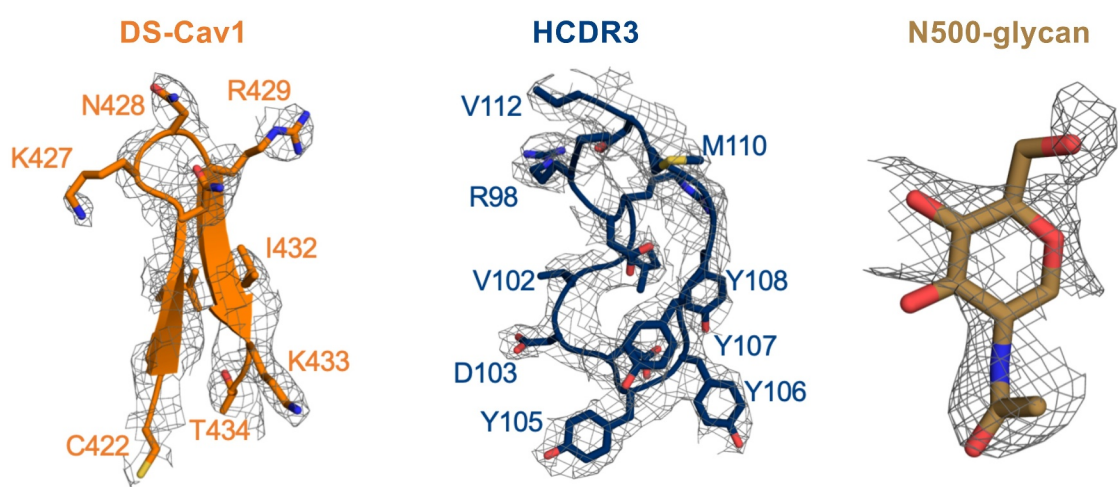


**Figure 3. Electron densities are highly comparable in X-ray and cryo-EM structures.** (a) Representative cryo-EM densities for regions of DS-Cav1 (left, orange cartoon and sticks), AM14 (center, dark blue cartoon, and sticks), and the N-linked glycan on DS-Cav1 Asn500 (right, sand cartoon, and sticks). Maps are contoured at  $6\sigma$ . (b) Representative  $2F_o - F_c$  x-ray electron densities for the same regions shown in a), contoured at  $1\sigma$ . For simplicity, HCDR3 residues are numbered according to the X-ray structure.

mechanism behind the Arg429 flexibility. Nonetheless, the intrinsic flexibility of amino acid residues on the surface of PreF is likely a contributing factor for the antigenicity for each of these antigenic sites.

AM14's ability to neutralize RSV A and B strains with similar potency is due to the high conservation of the AM14 epitope, and though AM14 requires PreF to be in a trimeric state for binding, the neutralization potency is comparable to antibodies such as D25, RSB1, and CR9501, which are also PreF specific but can bind monomeric PreF. Thus, locking F in the PreF state seems to be a more important attribute for neutralization than the oligomeric state recognized by the antibody. A large portion of the human neutralizing antibody response to RSV infections has been shown to be directed toward antigenic sites  $\emptyset$ , IV, and V, while antibodies targeting the trimer-specific AM14 epitope are less frequent.<sup>16</sup> Our

analysis explains the binding competition that AM14 has with site V (RSB1) and site IV (101F), with the latter epitope also being present on PostF. This may explain the low prevalence of AM14-like antibodies in human sera, as they are likely outcompeted not only by the immunodominant PreF epitopes but also by other neutralizing and non-neutralizing epitopes present on PostF.

Although no other human PreF trimer-specific mAbs have been isolated, a prefusion, trimer-specific epitope has recently been described for the llama-derived single-domain antibodies (VHHs) F-VHH-4 and F-VHH-L66.<sup>47</sup> The epitope lies adjacent to that of AM14 and encompasses antigenic site II of one F protomer and antigenic site IV of the neighboring F protomer. This may suggest that additional trimer-specific epitopes are also recognizable by the human antibody repertoire, but have yet to be discovered. As PreF-based vaccines

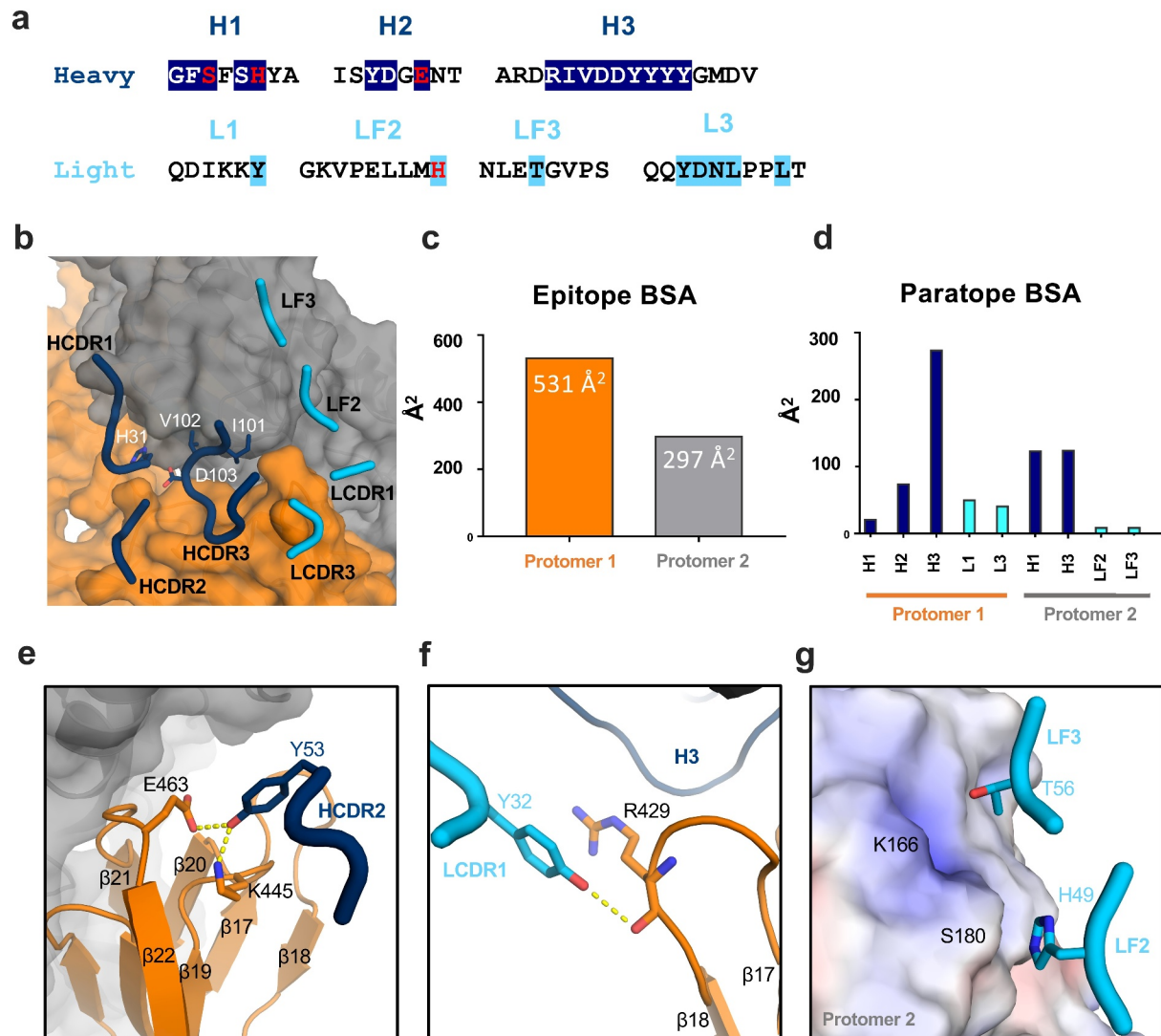


**Figure 4. AM14 heavy- and light-chain interactions identified from high-resolution structures solved herein.** (a) AM14 heavy- and light-chain CDRs and FRs which contact DS-Cav1. Residues which make hydrogen (h)-bonds or van der Waals' interactions are highlighted. Somatic hypermutations which contact DS-Cav1 are colored red. (b) AM14 heavy- and light-chain CDRs and light chain framework regions (LF) which contact the two DS-Cav1 protomers (protomer1 orange surface, protomer 2, gray surface). AM14 is shown as cartoon (dark blue-heavy chain, light blue-light chain) with residues bridging contacts between the two DS-Cav1 protomers shown as sticks. (d) AM14-buried paratope surface areas by CDR and LF regions of heavy and light chain per DS-Cav1 protomer. (e) Tyr53<sub>HCDR2</sub> forms H-bonds (yellow dashes) with DS-Cav1 protomer1 residues Lys 445 and Glu463. (f) Tyr32<sub>LCDR1</sub> traps Arg429 of DS-Cav1 protomer1 between the AM14 heavy and light chains. (g) LF regions 2 and 3 each bury a single residue on DS-Cav1 protomer 2, which is shown as electrostatic surface (blue: positive charges, red: negative charges, white: neutral).

continue to progress in clinical trials, it will be interesting to see how immunogenicity of the AM14 quaternary epitope contributes to vaccine-elicited antibody responses that no longer present PostF epitopes, and whether additional trimer-specific epitopes, such as those bound by the llama VHHs, will be unveiled. For this, recent advances in polyclonal epitope mapping methods, which allow to structurally characterize human antibody responses, might play a critical role.<sup>48–52</sup>

In summary, we report improved resolution structures of RSV prefusion F in its engineered stabilized version, known as DS-Cav1, in complex with Fab AM14, enabling comprehensive interpretation of important antibody–antigen interactions that were previously unappreciated at the available lower resolution. These structures serve as useful tools in understanding the molecular basis for trimer specificity, as well as in guiding the engineering of novel trimer-specific molecular probes or therapeutics to treat RSV infections.

## Materials and methods

### Expression and purification of DS-Cav1 and Fab AM14

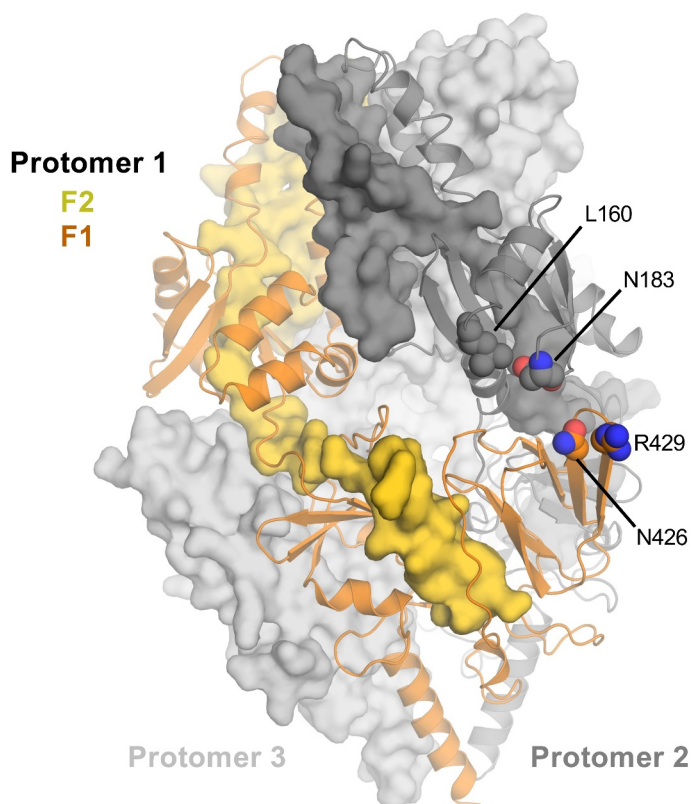
Un-tagged DS-Cav1 was produced in Chinese hamster ovary cells and purified by ion exchange and size exclusion chromatography, as previously reported.<sup>26</sup> Fab AM14 was expressed with a Strep Tag II at the heavy-chain C terminus and purified using a StrepTrap HP column (GE Healthcare). The tag was proteolytically cleaved using TEV protease (AcTEV protease, Thermo Fisher Scientific) prior to size exclusion chromatography.

### Crystallization of DS-Cav1-Fab AM14 Complex

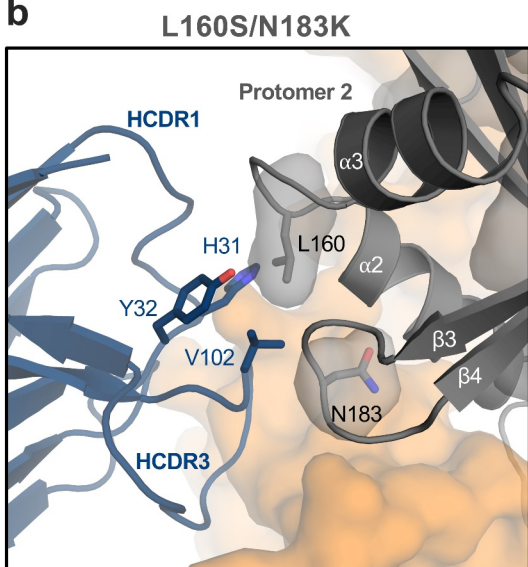
Purified DS-Cav1 was mixed at a 1:3.5 molar excess with Fab AM14 and stored at 4°C overnight to ensure full complex



a



b



c

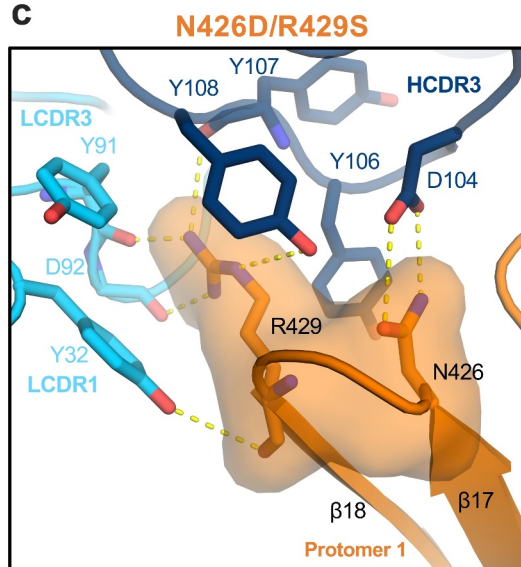


**Figure 5. Molecular basis for DS-Cav1 MARMs to AM14.** (a) Location of DS-Cav1 MARM residues L160, N183, N426, and R429 are shown as spheres. The DS-Cav1 protomer 1 is colored as orange cartoon for the F1 portion and gold surface for the F2 portion. Protomer 2 is colored in dark gray cartoon for the F2 portion and dark gray surface for F1, and protomer 3 is shown as light gray surface for F1 and F2. L160/N183 (b) and N426/R429 (c) with AM14 are shown with surface and dashed lines. DS-Cav1 and AM14 are shown as cartoon and colored as in a). Residues involved in interactions are shown as sticks for both DS-Cav1 and AM14 and depicted with semi-transparent surfaces for DS-Cav1, while H-bonds are depicted with dashed yellow lines.

formation (3 Fabs per DS-Cav1 trimer). DS-Cav1-FabAM14 complex were separated from excess Fab by size exclusion chromatography on a superdex 200 10/300 GL column with buffer 10 mM Hepes pH 7.5, 150 mM NaCl, and 5% glycerol. The fractions for the peak corresponding to DS-Cav1-FabAM14 complex were pooled and concentrated to 6 mg/

mL for crystal screening via sitting drop vapor diffusion at a 1:1 ratio of protein to screening buffer. Plates were incubated at room temperature in a Formulatrix Rock Imager 1000 and monitored/imaged for up to one month. DS-Cav1-FabAM14 crystals were identified in buffer containing 0.2 M NaCl, 0.1 M MES pH 6.0, 20% w/v PEG 2000 MME. Crystals were cryo-

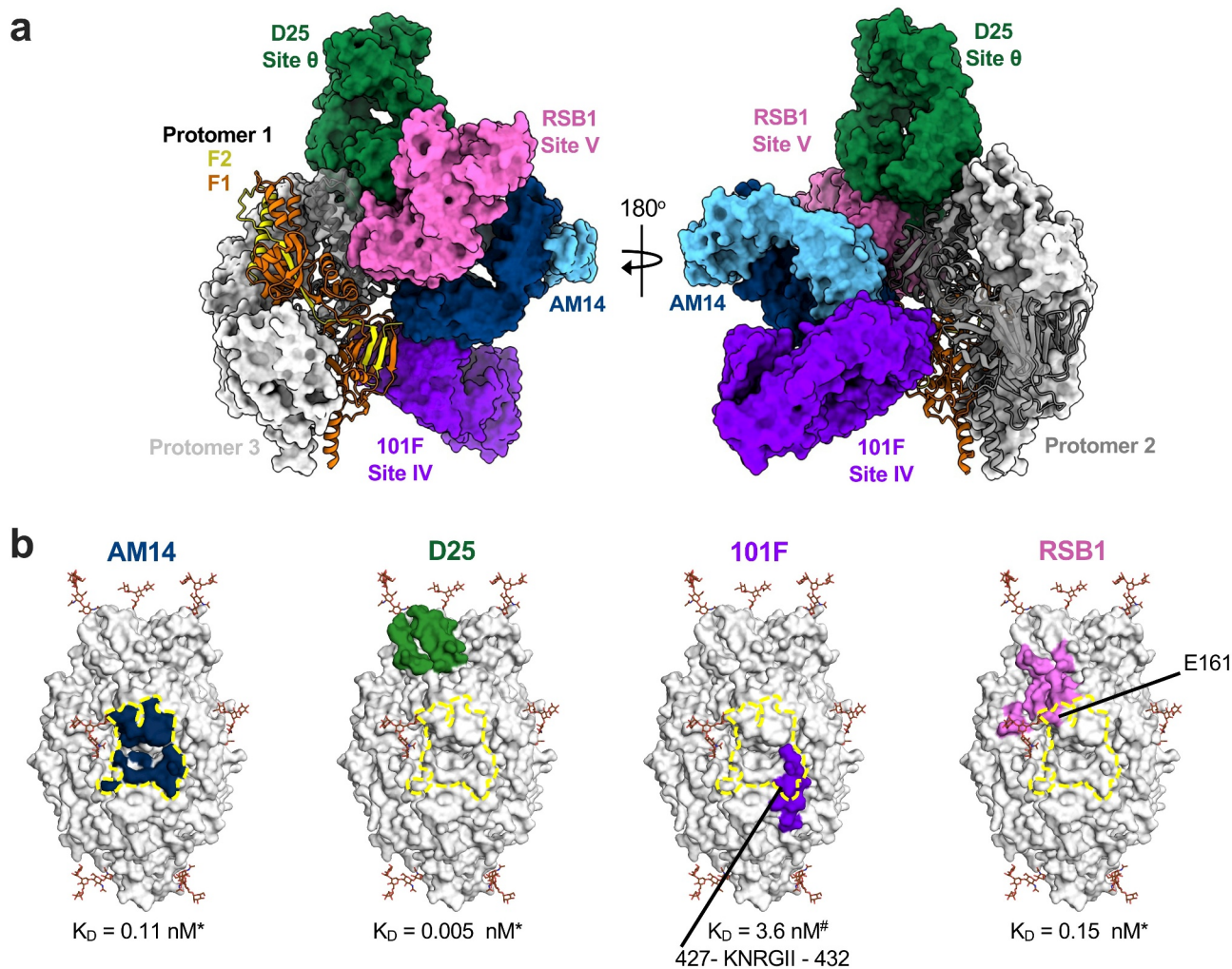


**Figure 6. AM14 competes with antigenic sites IV and V but not site  $\theta$ .** (a) X-ray structures for site V antibody RSB1 (PDB 6W52, pink surface), site IV antibody 101F (PDB 3O45, violet surface), and site  $\theta$  antibody D25 (PDB 4JHW, green surface) were superimposed onto the DS-Cav1-AM14 complex solved in this study (dark and light blue surfaces for AM14 heavy and light chains, respectively). For simplicity, only a single Fab for each antibody is shown bound to trimeric DS-Cav1, which is colored by protomer as in previous figures. (b) Surface representation of DS-Cav1 is colored white with the AM14 epitope colored dark blue and/or outlined with a dotted yellow line, the D25 epitope colored green, the 101F epitope colored purple, and the RSB1 epitope colored pink. Glycans are shown as sticks and were modeled using the Glyprot server.<sup>64\*</sup> Harshbarger et al., 2020. <sup>26</sup> McLellan et al., 2010<sup>27</sup>

protected in well solution supplemented with 10–20% ethylene glycol, flash-frozen and shipped to the Advanced Photon Source at Argonne National Labs for data collection.

### Crystal structure determination, model building, and refinement

DS-Cav1-FabAM14 crystals diffracted to a maximum resolution of 3.6 Å. Diffraction data were collected, indexed, and scaled into space group C2 using HKL2000,<sup>53</sup> and Phaser<sup>54</sup> was used for molecular replacement with PDB 4MMU as the search model for DS-Cav1 and PDB 4ZYK as the search model for AM14. A single trimer of DS-Cav1 was found in the asymmetric unit bound by three AM14 Fabs. Iterative rounds of reciprocal space and real space refinement were carried out in Phenix<sup>22</sup> and Coot.<sup>55</sup> The final structure yielded  $R_{\text{work}}$  and  $R_{\text{free}}$  values of 0.20 and 0.24, respectively (Table 1). Final coordinates were deposited in the Protein Data Bank with accession code 7MMN.

### Cryo-EM specimen preparation

Quantifoil Cu 300 mesh grids (Agar Scientific) were glow discharged (Pelco easiGlow) for 45 s at 25 mA. 3  $\mu\text{l}$  of DS-Cav1-FabAM14 sample at a concentration of  $\sim 0.5 \text{ mg/ml}$  was applied to the grid and immediately plunged into liquid ethane using an FEI Vitrobot Mark IV (FEI ThermoFisher) after blotting for 2.5 s, blot force at 2, at 4°C and  $\sim 100\%$  relative humidity.

### Cryo-EM data collection and image processing

Cryo-EM data were collected in movie mode on a FEI Titan Krios electron microscope operating at 300 kV and equipped with a Falcon III direct detector (Nanosciences Center, Cambridge University, UK) with a pixel size of 1.07 Å per super-resolution pixel. Each movie consisted of 75 frames collected over 60 s with an exposure per frame of 0.51  $e^-/\text{Å}^2$  giving a total exposure of 26.7  $e^-/\text{Å}^2$ . The applied defocus ranged between  $\sim 1.4$  and 3.4  $\mu\text{m}$  underfocus. A total number

of 1353 movie stacks with 75 frames were collected (Table 2). Image processing was performed in cisTEM.<sup>56</sup> The frames of each movie were aligned, dose-weighted, and summed into a single image, image defocus was determined using CTFFIND4<sup>57</sup> and images with excessive motion, low contrast, ice contamination, or poor power spectra were removed after visual inspection. 25,280 particles were automatically selected from aligned micrographs using a soft-edge disk template picking tool, and subsequently used for 2D classification. A total of 23,737 particles that produced usable 2D classes were then combined and subjected to *ab-initio* 3D reconstruction, which was then used for refinement resulting in a final map at 3.4 Å resolution, as determined by FSC with a 0.143 cutoff criterion.<sup>58</sup> Bloccres<sup>59</sup> was used to calculate and plot local resolutions, UCSF Chimera<sup>21</sup> was used for visualization, to invert handedness and generate segment and slab clip density.

### Cryo-EM model building, refinement, and analysis

The best-refined crystal structure of Ds-Cav1-AM14 was rigid-body fit into the 3.4 Å resolution cryo-EM map in UCSF Chimera.<sup>21</sup> Further iterative refinement cycles between the phenix.real\_space\_refine command in PHENIX<sup>60</sup> with secondary structure restraints and manual adjustments in COOT<sup>23</sup> yielded the final model. The quality of the refinement was assessed by the PHENIX cryo-EM validation tool.<sup>61,62</sup> All the refinement statistics are summarized in Table 2. Figures were generated using ChimeraX<sup>63</sup> and PyMOL (Schrödinger, LLC). EM density map and structure model are accessible through EMD-23933 and PDB 7MPG.<sup>64</sup>

### Acknowledgments

We thank Karen Matsuoka for expression, harvesting, and buffer exchange of culture supernatants. We thank Trissa Elkins and Robert Nolte for crystallography and computing support. This research used resources of the Advanced Photon Source, a U.S. Department of Energy (DOE) Office of Science User Facility operated for the DOE Office of Science by Argonne National Laboratory under Contract No. DE-AC02-06CH11357. Data were collected at Southeast Regional Collaborative Access Team (SER-CAT) 22-ID (or 22-BM) beamline at the Advanced Photon Source, Argonne National Laboratory. SER-CAT is supported by its member institutions (see [www.ser-cat.org/members.html](http://www.ser-cat.org/members.html)), and equipment grants (S10\_RR25528 and S10\_RR028976) from the National Institutes of Health.

### Data availability

Data supporting the findings of this manuscript are available from the corresponding authors upon reasonable request. The atomic coordinates and corresponding structure factors for the DS-Cav1-AM14 Fab X-ray structure have been deposited to the RCSB Protein Data Bank, PDB 7MMN. The Cryo-EM density map of the DS-Cav1-AM14 Fab complex has been deposited in the Electron Microscopy Data Bank, EMD-23933. The atomic coordinates for the Cryo-EM complex have been deposited to the RCSB Protein Data Bank, PDB 7MPG.

### Disclosure statement

All authors are/were employees of the GSK group of companies at the time of the study.

### Funding

This study was sponsored by GlaxoSmithKline Biologicals SA. The funder provided support in the form of salaries for all authors and provided support in the form of research material. GlaxoSmithKline Biologicals SA was involved in the study design, data collection and analysis, decision to publish, and preparation of the manuscript.

### ORCID

Wayne Harshbarger  <http://orcid.org/0000-0002-1673-0679>  
 Priyanka D. Abeyrathne  <http://orcid.org/0000-0002-6814-7637>  
 Sai Tian  <http://orcid.org/0000-0002-5309-240X>  
 Sumana Chandramouli  <http://orcid.org/0000-0001-6994-506X>  
 Matthew James Bottomley  <http://orcid.org/0000-0001-9734-5694>  
 Enrico Malito  <http://orcid.org/0000-0002-1669-5607>

### References

- Nair H, Nokes DJ, Gessner BD, Dherani M, Madhi SA, Singleton RJ, O'Brien KL, Roca A, Wright PF, Bruce N, et al. Global burden of acute lower respiratory infections due to respiratory syncytial virus in young children: a systematic review and meta-analysis. *Lancet*. 2010;375(9725):1545–55. doi:10.1016/S0140-6736(10)60206-1.
- Resch B. Burden of respiratory syncytial virus infection in young children. *World Journal of Clinical Pediatrics*. 2012;1(3):8–12. doi:10.5409/wjcp.v1.i3.8.
- Anderson LJ, Dormitzer PR, Nokes DJ, Rappuoli R, Roca A, Graham BS. Strategic priorities for respiratory syncytial virus (rsv) vaccine development. *Vaccine*. 2013;31(2):B209–215. doi:10.1016/j.vaccine.2012.11.106.
- Higgins D, Trujillo C, Keech C. Advances in rsv vaccine research and development - a global agenda. *Vaccine*. 2016;34(26):2870–75. doi:10.1016/j.vaccine.2016.03.109.
- Rossey I, McLellan JS, Saelens X, Schepens B. Clinical potential of prefusion rsv f-specific antibodies. *Trends Microbiol*. 2018;26(3):209–19. doi:10.1016/j.tim.2017.09.009.
- McLellan JS, Chen M, Leung S, Graepel KW, Du X, Yang Y, Zhou T, Baxa U, Yasuda E, Beaumont T, et al. Structure of rsv fusion glycoprotein trimer bound to a prefusion-specific neutralizing antibody. *Science*. 2013;340(6136):1113–17. doi:10.1126/science.1234914.
- Rossey I, Saelens X. Vaccines against human respiratory syncytial virus in clinical trials. Where are We Now? *Expert Rev Vaccines*. 2019;18(10):1053–67. doi:10.1080/14760584.2019.1675520.
- McLellan JS, Chen M, Joyce MG, Sastry M, Stewart-Jones GB, Yang Y, Zhang B, Chen L, Srivatsan S, Zheng A, et al. Structure-based design of a fusion glycoprotein vaccine for respiratory syncytial virus. *Science*. 2013;342(6158):592–98. doi:10.1126/science.1243283.
- Falloon J, Yu J, Esser MT, Villafana T, Yu L, Dubovsky F, Takas T, Levin MJ, Falsey AR. An Adjuvanted, Postfusion F Protein-Based Vaccine Did Not Prevent Respiratory Syncytial Virus Illness in Older Adults. *J Infect Dis*. 2017;216(11):1362–70. doi:10.1093/infdis/jix503.
- Crank MC, Ruckwardt TJ, Chen M, Morabito KM, Phung E, Costner PJ, Holman LA, Hickman SP, Berkowitz NM, Gordon IJ, et al. A proof of concept for structure-based vaccine design targeting rsv in humans. *Science*. 2019;365(6452):505–09. doi:10.1126/science.aav9033.
- Ngwuta JO, Chen M, Modjarrad K, Joyce MG, Kanekiyo M, Kumar A, Yassine HM, Moin SM, Killikelly AM, Chuang GY et al. Prefusion f-specific antibodies determine the magnitude of rsv neutralizing activity in human sera. *Sci Transl Med* 2015;7(309): 309ra162. doi:10.1126/scitranslmed.aac4241
- LJ C, Gonzalez-Reyes L, Garcia-Barreno B, Sa W, Jj S, Dc W, Ja M. Electron microscopy of the human respiratory syncytial virus fusion protein and complexes that it forms with monoclonal

- antibodies. *Virology*. 2000;271(1):122–31. doi:10.1006/viro.2000.0279.
13. Magro M, Andreu D, Gomez-Puertas P, Melero JA, Palomo C. Neutralization of human respiratory syncytial virus infectivity by antibodies and low-molecular-weight compounds targeted against the fusion glycoprotein. *J Virol*. 2010;84(16):7970–82. doi:10.1128/JVI.00447-10.
  14. McLellan JS. Neutralizing epitopes on the respiratory syncytial virus fusion glycoprotein. *Curr Opin Virol*. 2015;11:70–75. doi:10.1016/j.coviro.2015.03.002.
  15. Taylor G, Stott EJ, Furze J, Ford J, Sopp P. Protective epitopes on the fusion protein of respiratory syncytial virus recognized by murine and bovine monoclonal antibodies. *J Gen Virol*. 1992;73(Pt 9):2217–23. doi:10.1099/0022-1317-73-9-2217.
  16. Gilman MS, Castellanos CA, Chen M, Ngwuta JO, Goodwin E, Moin SM, Mas V, Melero JA, Wright PF, Graham BS, et al. Rapid profiling of rsv antibody repertoires from the memory b cells of naturally infected adult donors. *Sci Immunol*. 2016;1(6):eaaj1879–eaaj1879. doi:10.1126/sciimmunol.aaj1879.
  17. Graham BS. Immunological goals for respiratory syncytial virus vaccine development. *Curr Opin Immunol*. 2019;59:57–64. doi:10.1016/j.coi.2019.03.005.
  18. Kwakkenbos MJ, Diehl SA, Yasuda E, Bakker AQ, van Geelen CM, Lukeni MV, van Bleek GM, Widjoatmodjo MN, Bogers WM, Mei H, et al. Generation of stable monoclonal antibody-producing b cell receptor-positive human memory b cells by genetic programming. *Nat Med*. 2010;16(1):123–28. doi:10.1038/nm.2071.
  19. Gilman MS, Moin SM, Mas V, Chen M, Patel NK, Kramer K, Zhu Q, Kabeche SC, Kumar A, Palomo C, et al. Characterization of a prefusion-specific antibody that recognizes a quaternary, cleavage-dependent epitope on the rsv fusion glycoprotein. *PLoS Pathog*. 2015;11(7):e1005035. doi:10.1371/journal.ppat.1005035.
  20. Malito E, Carfi A, Bottomley MJ. Protein crystallography in vaccine research and development. *Int J Mol Sci*. 2015;16(6):13106–40. doi:10.3390/ijms160613106.
  21. Pettersen EF, Goddard TD, Huang CC, Couch GS, Greenblatt DM, Meng EC, Ferrin TE. UCSF Chimera?A visualization system for exploratory research and analysis. *J Comput Chem*. 2004;25(13):1605–12. doi:10.1002/jcc.20084.
  22. Adams PD, Afonine PV, Bunkoczi G, Chen VB, Davis IW, Echols N, Headd JJ, Hung LW, Kapral GJ, Grosse-Kunstleve RW, et al. Phenix: a comprehensive python-based system for macromolecular structure solution. *Acta Crystallogr D Biol Crystallogr*. 2010;66(Pt 2):213–21. doi:10.1107/S0907444909052925.
  23. Emsley P, Cowtan CK. Coot: model-building tools for molecular graphics. *Acta Crystallogr D Biol Crystallogr*. 2004;60(12):2126–32. doi:10.1107/S0907444904019158.
  24. Krissinel E, Henrick K. Inference of macromolecular assemblies from crystalline state. *J Mol Biol*. 2007;372(3):774–97. doi:10.1016/j.jmb.2007.05.022.
  25. Giudicelli V, Duroux P, Ginestoux C, Folch G, Jabado-Michaloud J, Chaume D, Lefranc MP. Imgt/ligm-db, the imgt comprehensive database of immunoglobulin and t cell receptor nucleotide sequences. *Nucleic Acids Res*. 2006;34(Database issue):D781–784. doi:10.1093/nar/gkj088.
  26. Harshbarger W, Tian S, Wahome N, Balsaraf A, Bhattacharya D, Jiang D, Pandey R, Tungare K, Friedrich K, Mehzabeen N, et al. Convergent structural features of respiratory syncytial virus neutralizing antibodies and plasticity of the site v epitope on prefusion f. *PLoS Pathog*. 2020;16(11):e1008943. doi:10.1371/journal.ppat.1008943.
  27. McLellan JS, Chen M, Chang J-S, Yang Y, Kim A, Graham BS, Kwong PD. Structure of a major antigenic site on the respiratory syncytial virus fusion glycoprotein in complex with neutralizing antibody 101f. *J Virol*. 2010;84(23):12236–44. doi:10.1128/JVI.01579-10.
  28. Huang J, Diaz D, Mousa JJ. Antibody epitopes of pneumovirus fusion proteins. *Front Immunol*. 2019;10:2778. doi:10.3389/fimmu.2019.02778.
  29. Arbiza J, Taylor G, Lopez JA, Furze J, Wyld S, Whyte P, Stott EJ, Wertz G, Sullender W, Trudel M, et al. Characterization of two antigenic sites recognized by neutralizing monoclonal antibodies directed against the fusion glycoprotein of human respiratory syncytial virus. *J Gen Virol*. 1992;73(9):2225–34. doi:10.1099/0022-1317-73-9-2225.
  30. Lopez JA, Bustos R, Orvell C, Berois M, Arbiza J, Garcia-Barreno B, Melero JA. Antigenic structure of human respiratory syncytial virus fusion glycoprotein. *J Virol*. 1998;72(8):6922–28. doi:10.1128/JVI.72.8.6922-6928.1998.
  31. Biagi C, Dondi A, Scarpini S, Rocca A, Vandini S, Poletti G, Lanari M. Current state and challenges in developing respiratory syncytial virus vaccines. *Vaccines (Basel)*. 2020;8:4.
  32. Yuan M, Cottrell CA, Ozorowski G, van Gils MJ, Kumar S, Wu NC, Sarkar A, Torres JL, De Val N, Copps J, et al. Conformational plasticity in the hiv-1 fusion peptide facilitates recognition by broadly neutralizing antibodies. *Cell Host Microbe*. 2019;25(6):873–883 e875. doi:10.1016/j.chom.2019.04.011.
  33. Stanfield RL, Berndsen ZT, Huang R, Sok D, Warner G, Torres JL, Burton DR, Ward AB, Wilson IA, Smider VV. Structural basis of broad hiv neutralization by a vaccine-induced cow antibody. *Sci Adv*. 2020;6(22):eaba0468. doi:10.1126/sciadv.aba0468.
  34. Rantalainen K, Berndsen ZT, Antanasijevic A, Schiffner T, Zhang X, Lee W-H, Torres JL, Zhang L, Irimia A, Copps J, et al. Hiv-1 envelope and mper antibody structures in lipid assemblies. *Cell Rep*. 2020;31(4):107583. doi:10.1016/j.celrep.2020.107583.
  35. Pan J, Peng H, Chen B, Harrison SC. Cryo-em structure of full-length hiv-1 env bound with the fab of antibody pg16. *J Mol Biol*. 2020;432(4):1158–68. doi:10.1016/j.jmb.2019.11.028.
  36. Bartesaghi A, Merk A, Borgnia MJ, Milne JL, Subramaniam S. Prefusion structure of trimeric hiv-1 envelope glycoprotein determined by cryo-electron microscopy. *Nat Struct Mol Biol*. 2013;20(12):1352–57. doi:10.1038/nsmb.2711.
  37. Zhu X, Turner HL, Lang S, McBride R, Bangaru S, Gilchuk IM, Yu W, Paulson JC, Crowe JE Jr., Ward AB, et al. Structural basis of protection against h7n9 influenza virus by human anti-n9 neuraminidase antibodies. *Cell Host Microbe*. 2019;26(6):729–738 e724. doi:10.1016/j.chom.2019.10.002.
  38. Turner HL, Pallesen J, Lang S, Bangaru S, Urata S, Li S, Cottrell CA, Bowman CA, Crowe JE Jr., Wilson IA, et al. Potent anti-influenza h7 human monoclonal antibody induces separation of hemagglutinin receptor-binding head domains. *PLoS Biol*. 2019;17(2):e3000139. doi:10.1371/journal.pbio.3000139.
  39. Liu Y, Pan J, Jenni S, Raymond DD, Caradonna T, Do KT, Schmidt AG, Harrison SC, Grigorieff N. CryoEM Structure of an Influenza Virus Receptor-Binding Site Antibody–Antigen Interface. *J Mol Biol*. 2017;429(12):1829–39. doi:10.1016/j.jmb.2017.05.011.
  40. Benton DJ, Nans A, Calder LJ, Turner J, Neu U, Lin YP, Ketelaars E, Kallewaard NL, Corti D, Lanzavecchia A, et al. Influenza hemagglutinin membrane anchor. *Proc Natl Acad Sci U S A*. 2018;115(40):2217–23. doi:10.1073/pnas.1810927115.
  41. Wirawan M, Fibriansah G, Marzinek JK, Lim XX, Ng TS, Sim AYL, Zhang Q, Kostyuchenko VA, Shi J, Smith SA, et al. Mechanism of enhanced immature dengue virus attachment to endosomal membrane induced by prm antibody. *Structure*. 2019;27(2):253–267 e258. doi:10.1016/j.str.2018.10.009.
  42. Fibriansah G, Lim EXY, Marzinek JK, Ng T-S, Tan JL, Huber RG, Lim X-N, Chew VSY, Kostyuchenko VA, Shi J, et al. Antibody affinity versus dengue morphology influences neutralization. *PLoS Pathog*. 2021;17(2):e1009331. doi:10.1371/journal.ppat.1009331.
  43. Fibriansah G, Ibarra KD, Ng TS, Smith SA, Tan JL, Lim XN, Ooi JS, Kostyuchenko VA, Wang J, De Silva AM, et al. Dengue virus. Cryo-em structure of an antibody that neutralizes dengue virus type 2 by locking e protein dimers. *Science*. 2015;349(6243):88–91. doi:10.1126/science.aaa8651.
  44. Xie Q, Wang Z, Ni F, Chen X, Ma J, Patel N, Lu H, Liu Y, Tian J-H, Flyer D, et al. Structure basis of neutralization by a novel site ii/iv

- antibody against respiratory syncytial virus fusion protein. *PLoS One*. 2019;14(2):e0210749. doi:10.1371/journal.pone.0210749.
45. Mukhamedova M, Wrapp D, Shen CH, Gilman MSA, Ruckwardt TJ, Schramm CA, Ault L, Chang L, Derrien-Colemyan A, Lucas SAM, et al. Vaccination with prefusion-stabilized respiratory syncytial virus fusion protein induces genetically and antigenically diverse antibody responses. *Immunity*. 2021;54(4):769–780 e766. doi:10.1016/j.immuni.2021.03.004.
  46. Paul F, Weikl TR. How to distinguish conformational selection and induced fit based on chemical relaxation rates. *PLoS Comput Biol*. 2016;12(9):e1005067. doi:10.1371/journal.pcbi.1005067.
  47. Rossey I, Gilman MS, Kabeche SC, Sedeyn K, Wrapp D, Kanekiyo M, Chen M, Mas V, Spitaels J, Melero JA, et al. Potent single-domain antibodies that arrest respiratory syncytial virus fusion protein in its prefusion state. *Nat Commun*. 2017;8(1):14158. doi:10.1038/ncomms14158.
  48. Ward AB, Wilson IA. Innovations in structure-based antigen design and immune monitoring for next generation vaccines. *Curr Opin Immunol*. 2020;65:50–56. doi:10.1016/j.coi.2020.03.013.
  49. Nogal B, Bianchi M, Cottrell CA, Kirchdoerfer RN, Sewall LM, Turner HL, Zhao F, Sok D, Burton DR, Hangartner L, et al. Mapping polyclonal antibody responses in non-human primates vaccinated with hiv env trimer subunit vaccines. *Cell Rep*. 2020;30(11):3755–3765 e3757. doi:10.1016/j.celrep.2020.02.061.
  50. Han J, Schmitz AJ, Richey ST, Dai Y-N, Turner HL, Mohammed BM, Fremont DH, Ellebedy AH, Ward AB. Polyclonal epitope mapping reveals temporal dynamics and diversity of human antibody responses to h5n1 vaccination. *Cell Rep*. 2021;34(4):108682. doi:10.1016/j.celrep.2020.108682.
  51. Dingens AS, Pratap P, Malone K, Hilton SK, Ketas T, Cottrell CA, Overbaugh J, Moore JP, Klasse PJ, Ward AB, et al. High-resolution mapping of the neutralizing and binding specificities of polyclonal sera post-hiv env trimer vaccination. *Elife*. 2021;10:e64281. doi:10.7554/eLife.64281.
  52. Bianchi M, Turner HL, Nogal B, Cottrell CA, Oyen D, Pauthner M, Bastidas R, Nedellec R, McCoy LE, Wilson IA, et al. Electron-microscopy-based epitope mapping defines specificities of polyclonal antibodies elicited during hiv-1 bg505 envelope trimer immunization. *Immunity*. 2018;49(2):288–300 e288. doi:10.1016/j.immuni.2018.07.009.
  53. Minor W, Cymborowski M, Otwinowski Z, Chruszcz M. HKL-3000: the integration of data reduction and structure solution – from diffraction images to an initial model in minutes. *Acta Crystallogr D Biol Crystallogr*. 2006;62(8):859–66. doi:10.1107/S0907444906019949.
  54. McCoy AJ, Grosse-Kunstleve RW, Adams PD, Winn MD, Storoni LC, Read RJ. Phaser crystallographic software. *J Appl Crystallogr*. 2007;40(Pt 4):658–74. doi:10.1107/S0021889807021206.
  55. Emsley P, Lohkamp B, Scott WG, Cowtan K. Features and development of Coot. *Acta Crystallogr D Biol Crystallogr*. 2010;66(4):486–501. doi:10.1107/S0907444910007493.
  56. Grant T, Rohou A, Grigorieff N. Cistem, user-friendly software for single-particle image processing. *Elife*. 2018;7:e35383. doi:10.7554/eLife.35383.
  57. Rohou A, Ctfind GN. Fast and accurate defocus estimation from electron micrographs. *J Struct Biol*. 2015;192(2):216–21. doi:10.1016/j.jsb.2015.08.008.
  58. Rosenthal PB, Henderson R. Optimal determination of particle orientation, absolute hand, and contrast loss in single-particle electron cryomicroscopy. *J Mol Biol*. 2003;333(4):721–45. doi:10.1016/j.jmb.2003.07.013.
  59. Cardone G, Heymann JB, Steven AC. One number does not fit all: mapping local variations in resolution in cryo-em reconstructions. *J Struct Biol*. 2013;184(2):226–36. doi:10.1016/j.jsb.2013.08.002.
  60. Afonine PV, Poon BK, Read RJ, Sobolev OV, Terwilliger TC, Urzhumtsev A, Adams PD. Real-space refinement in PHENIX for cryo-EM and crystallography. *Acta Crystallographica Section D Structural Biology*. 2018;74(6):531–44. doi:10.1107/S2059798318006551.
  61. Afonine PV, Klaholz BP, Moriarty NW, Poon BK, Sobolev OV, Terwilliger TC, Adams PD, Urzhumtsev A. New tools for the analysis and validation of cryo-em maps and atomic models. *Acta Crystallogr D Struct Biol*. 2018;74(Pt 9):814–40. doi:10.1107/S2059798318009324.
  62. Williams CJ, Headd JJ, Moriarty NW, Prisant MG, Videau LL, Deis LN, Verma V, Keedy DA, Hintze BJ, Chen VB, et al. Molprobity: more and better reference data for improved all-atom structure validation. *Protein Sci*. 2018;27(1):293–315. doi:10.1002/pro.3330.
  63. Goddard TD, Huang CC, Meng EC, Pettersen EF, Couch GS, Morris JH, Ferrin TE. Ucsf chimeraX: meeting modern challenges in visualization and analysis. *Protein Sci*. 2018;27(1):14–25. doi:10.1002/pro.3235.
  64. Bohne-Lang A, von der Lieth C-W. Glyprot: in silico glycosylation of proteins. *Nucleic Acids Res*. 2005;33(Web Server):W214–219. doi:10.1093/nar/gki385.